Peer-reviewed version available at *Energies* **2019**, *12*, 3900; doi:10.3390/en12203900

Article

A modified free wake vortex ring method for horizontal-axis wind turbines

Jing Dong [1]*, Axelle Viré [1], Carlos Simao Ferreira[1], Zhangrui Li[2] and Gerard van Bussel [1]

[1] Faculty of Aerospace Engineering, Delft University of Technology, Kluyverweg 1, 2629 HS, Delft, The Netherlands.
[2] Wind Energy Group, Shanghai Electric Group Company Limited, Shanghai, China.
* Correspondence: J.Dong-2@tudelft.nl; Tel.:+31-616461999

Abstract: A modified free-wake vortex ring model is proposed to compute the dynamics of a floating horizontal-axis wind turbine. The model is divided into two parts. The near wake model uses a blade bound vortex model and trailed vortex model, which is developed based on vortex filament method. By contrast, the far wake model is based on the vortex ring method. The proposed model is a good compromise between accuracy and computational cost, for example when compared with more complex vortex methods. The present model is used to assess the influence of floating platform motions on the performance of a horizontal-axis wind turbine rotor. The results are validated on the 5MW NREL rotor and compared with other aerodynamic models for the same rotor subjected to different platform motions. It was found that the results from the proposed method are more reliable than the results from BEM theory especially at small angles of attack in the region of low wind speeds, on the one hand, and high wind speeds with blade pitch motions, on the other hand. And also the proposed method is less time consuming and has similar accuracy when comparing with more advanced vortex based methods.

Keywords: free wake vortex method, horizontal-axis wind turbine, floating wind energy, aerodynamics

1. Introduction

It has been shown by Sebastian[1] that the unsteady aerodynamic loads experienced by floating offshore wind turbines (FOWTs) can be significantly different than for bottom-fixed wind turbines. Simulation tools that can accurately evaluate the relationship between the aerodynamic loads on the rotor and the platform motion are required especially for off-design conditions or novel concepts. So far, the available aero-hydro coupled analysis tools are almost exclusively based on the blade element momentum (BEM) theory, which describes the steady state behavior of a wind turbine and has been proved to be unsuitable when the rotor interacts with its own wake, as it is the case for FOWTs. An alternative is to use computational fluid dynamics (CFD) models that describe the flow physics around the rotor with higher fidelity. However, they are computationally expensive when dealing with the fully-coupled dynamics of FOWTs. Another approach, that is more accurate than momentum theory and less costly than CFD, is the so-called vortex methods. Vorticity-based methods have a number of different formulations, ranging from simple analytical models to more advanced numerical methods (Branland [2]). Also the computational cost of vortex models depends on the number of vortex elements and the interaction between the elements, ranging from relatively cheap models to more expensive ones (Bhagwat[3],Gohard[4]). Since the rotating wind turbines generate bounded circulations on the blades and release vorticity into the wake, the vortex based methods are naturally suitable for the simulation of wind turbine aerodynamics. The blade vorticity is assumed to be concentrated on lifting lines, with distributed vortex strengths representing the bound circulation. The vorticity is then convected to the wake as shed and trailed vorticity. The shed vorticity is the vorticity emitted in the wake due to time change of the bound circulation, whilst the

Peer-reviewed version available at Energies 2019, 12, 3900; doi:10.3390/en12203900

trailed vorticity results from the spanwise change of bound circulation (Branland [2]). Within the scope of simplified vorticity models for rotors, the wake flow can be represented by vortex filaments such as the free wake vortex filament (FWVF) method of Sebastian[5], vortex particles such as the nonlinear vortex lattice method (NVLM) method of Lee [6], or a vortex ring model. As for the vortex ring methods, the wake is modeled by vortex rings, each carrying a constant circulation determined by the aerodynamic loads on the rotor. Each ring is a vortex element which induces velocity on both the rotor and the other rings in the field. Thus, the radius and spacing of the rings vary as the move downstream in the wake. This is the so-called free wake vortex ring method. In this method, the analytical solution of the induced velocity of an axisymmetric vortex ring derived from Biot-Savart law (Newman[7],Yoon[8]) can be directly used to calculate the induced velocities in the wake as well as on the rotor. This reduces computation cost whilst retaining the basic physical properties in the wake.

The simplest vortex ring methods available in the literature represent the rotor with an actuator disc, whilst the wake is modelled as vortex rings released at the tip of the rotor (Øye[9], de Vaal[10], Yu[11]). These models were used to calculate unsteady aerodynamic loads on both fixed and moving rotors. However, some aerodynamic features such as angle of attack, and lift and drag forces on the rotor could not be accurately reproduced due to the limitations associated with the actuator disc concept. A modeling method that represents the rotor blades with lifting lines, the near wake as a series of straight vortex lines and the far wake by vortex rings was initially suggested by Miller [12], relating the blade bound vortex strength with the vortex ring strength in the wake. In that case, the rotor loads were also dependent on the induced velocities from the vortex rings. Afjeh[13] and de Vaal [14] [15] adapted and improved this method to the modeling of wind turbines, and good agreement were achieved when comparing the numerical results with measurement data.

The free wake vortex ring method (FWVR) discussed in this paper is based on that initially proposed by de Vaal [15] and is applied to the aerodynamic analysis of a horizontal-axis wind turbine. It combines the three dimensional vortex lifting law with the blade element theory, which can accurately and effectively predict the blade load using the time-evolution of the induced velocities. It also splits the wake into near wake and far wake, leading to more realistic velocities on the blade and in the far-field. However, the application of de Vaal's original method [15] can be challenging for some working states. This is for example the case of small or negative angles of attack at low wind speeds, or blade pitching motions at high wind speeds. In this paper, we present a few modifications of the original method to overcome these challenges. First, the propagation process of the vortex rings is modified and different nonlinear iteration methods are tested to solve the blade bound vortex strengths. Second, the near-wake trailed vortex model uses finite length of vortex segments instead of semi-infinite vortex lines, which makes the near wake model physically more realistic.

The paper also discusses the transition between near- and far-wake models, as well as the calculation of the self-induced velocity. The proposed free wake vortex model is validated by analyzing the aerodynamic parameters on the NREL 5MW wind turbine with a bottom-mounted monopile foundation as well as floating platforms with prescribed rigid body motions, that are typical of wave induced motions for different types of floating foundations, i.e. ITI barge, OC3-Hywind spar-buoy (OHS), and tension leg platform (TLP). Results are compared with those obtained from the blade element momentum (BEM) theory, Reynolds-averaged Navier–Stokes (RANS) method of Sørensen[**?**] and two more computationally expensive vortex based aerodynamic models- the FWVF method of Sebastian[5] and the NVLM method of Lee [6].

The paper is organized as follows. The theory of the modified free wake vortex ring method is described in Section 2. The numerical modeling method is described and validated in Section 3. The computational time evaluation is shown in Section 4. The wind turbine aerodynamic analysis is

shown in Section 5. Finally, the conclusion are drawn in Section 6.

2. Vortex Ring Theory

The simplified free wake vortex ring method discussed in this paper is based on the model derived by de Vaal [14], which consists of two parts: the near wake model and the far wake model. The induced velocities of the near wake model are calculated based on Biot-Savart's law, as described in section 2.1. To keep a low computational cost, the far wake model is represented by the axisymmetric vortex rings as introduced in section 2.2.

2.1. Velocity induced by a vortex filament

The velocity $\mathbf{V}_P$ induced by a vortex filament with a constant strength Γ in the field at a point P can be expressed by Biot-Savart law as [16]

$$\mathbf{V}_P = -\frac{\Gamma}{4\pi}\int_{C(q)} \frac{\mathbf{r}_P - \mathbf{r}_q}{|\mathbf{r}_P - \mathbf{r}_q|^3} \times \frac{\partial \mathbf{r}_q}{\partial q} dq, \tag{1}$$

where $C(q)$ is the parametric curve which described the path of the vortex filament, $\mathbf{r}_P$ is the position vector of the point P, $\mathbf{r}_q$ is the position vector of a point Q on the filament, $\mathbf{r} = \mathbf{r}_P - \mathbf{r}_q$ is the vector pointing from point Q to point P, and $\frac{\partial \mathbf{r}_q}{\partial q}$ is the partial derivative of $\mathbf{r}_q$ with respect to the filament parameter. In Eq. (1) the kernel of Biot-Savart operator is identified as

$$\mathbf{K}(\mathbf{r}) = -\frac{1}{4\pi}\frac{\mathbf{r}}{|\mathbf{r}|^3}, \tag{2}$$

and it is singular when the point P is on the vortex filament $C(q)$. To avoid this singularity problem, a smoothing method proposed by Hoydonck *et al* [17] is used. It replaces the singular Biot-Savart kernel $\mathbf{K}(\mathbf{r})$ with a desingularized kernel $\mathbf{K}_\sigma(\mathbf{r})$, defined as

$$\mathbf{K}_\sigma(\mathbf{r}) = -\frac{g(\sigma)}{|\mathbf{r}|^3}\mathbf{r}, \tag{3}$$

where σ is the non-dimensionalised length between the point P and a point on the filament, and $g(\sigma)$ is a three-dimensional velocity smoothing function [17]. Here, the Rosenhead-Moore velocity smoothing function is used, i.e.

$$g(\sigma) = \frac{\sigma^3}{4\pi(\sigma^2+1)^{\frac{3}{2}}}. \tag{4}$$

This leads to the following induction velocity,

$$\mathbf{V}_P = \Gamma\int_{C(q)} \mathbf{K}_\sigma(\mathbf{r}) \times \frac{\partial \mathbf{r}_q}{\partial q} dq. \tag{5}$$

Considering a straight line vortex filament, the parametric curve of the filament is given by $\mathbf{C}(q) = \mathbf{x}_1 + q(\mathbf{x}_2 - \mathbf{x}_1)$, with $0 \le q \le 1$. Thus the desingularized kernel $\mathbf{K}_\sigma(\mathbf{r})$ can be expressed as

$$\mathbf{K}_\sigma(\mathbf{r}) = -\frac{\mathbf{x}_P - \mathbf{C}(q)}{4\pi(|\mathbf{x}_P - \mathbf{C}(q)|^2 + r_c^2)^{\frac{3}{2}}} = -\frac{\mathbf{x}_P - (1-q)\mathbf{x}_1 + q\mathbf{x}_2}{4\pi(|\mathbf{x}_P - (1-q)\mathbf{x}_1 + q\mathbf{x}_2|^2 + r_c^2)^{\frac{3}{2}}},. \tag{6}$$

where r_c is the vortex core radius. Accordingly, the induced velocity $\mathbf{V}_P$ can be expressed as

$$\mathbf{V}_P = -\Gamma \int_0^1 \frac{\mathbf{x}_P - (1-q)\mathbf{x}_1 + q\mathbf{x}_2}{4\pi(|\mathbf{x}_P - (1-q)\mathbf{x}_1 + q\mathbf{x}_2|^2 + r_c^2)^{\frac{3}{2}}} \times (\mathbf{x}_2 - \mathbf{x}_1)dq. \tag{7}$$

When the point x_2 extents to infinity, the straight line vortex filament becomes a semi-infinite line. In this case, the upper limit of $q = \widetilde{q}$ extends to infinity, and the induced velocity $\mathbf{V}_P$ becomes

$$\mathbf{V}_P = -\Gamma \lim_{\widetilde{q}\to\infty} f(q), \tag{8}$$

$$f(q) = \int_0^{\widetilde{q}} \frac{\mathbf{x}_P - (1-q)\mathbf{x}_1 + q\mathbf{x}_2}{4\pi(|\mathbf{x}_P - (1-q)\mathbf{x}_1 + q\mathbf{x}_2|^2 + r_c^2)^{\frac{3}{2}}} \times (\mathbf{x}_2 - \mathbf{x}_1)dq. \tag{9}$$

2.2. Velocity induced by an axis-symmetric vortex ring

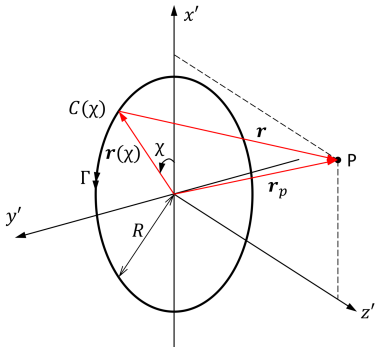

Figure 1. Coordinate system associated with a vortex ring.

Considering an ideal vortex ring with radius R as shown in Figure 1, its parametric curve $C(\chi)$ with the angle χ as the parametrisation parameter can be expressed as

$$C(\chi) = R(\cos\chi, \sin\chi, 0), \qquad \chi \in [0, 2\pi]. \tag{10}$$

Since the vortex ring is axis-symmetric, its local vortex ring coordinate system $x'y'z'$ can be adjusted according to the location of the field point P. Here, the coordinates of P are $(x'_P, 0, z'_P)$ and $C(\chi)$ is in the $x'y'$-plane and centered at the origin of the z'-axis. Thus, taking the notation $x'_P = \eta R$ and $z'_P = \zeta R$, we have

$$\mathbf{r}(\chi) = R(\cos\chi, \sin\chi, 0), \tag{11}$$

$$\mathbf{r}_P = R(\eta, 0, \zeta), \qquad \eta \in (0, +\infty), \zeta \in (-\infty, +\infty). \tag{12}$$

The displacement vector $\mathbf{r}$ is thus given by

$$\mathbf{r} = \mathbf{r}_P - \mathbf{r}(\chi) = R(\eta - \cos\chi, -\sin\chi, \zeta). \tag{13}$$

The velocity induced by a vortex ring at a point P is then obtained by substituting the above equations into Eq. (5), which yields:

$$\mathbf{V} = -\frac{\Gamma}{4\pi R} \int_0^{2\pi} \frac{(\zeta\cos\chi, \zeta\sin\chi, 1 - \eta\cos\chi)}{(1 + \eta^2 + \zeta^2 + \sigma^2 - 2\eta\cos\chi)^{\frac{3}{2}}} d\chi, \tag{14}$$

An analytical result of this integral has been derived as [7][8]

$$V_x = \frac{\Gamma}{2\pi R C_0}\left[-K(m) + \frac{1+\eta^2+\zeta^2}{C_1^2}E(m)\right]\frac{\zeta}{\eta}, \tag{15}$$

$$V_z = \frac{\Gamma}{2\pi R C_0}\left[K(m) + \frac{1-\eta^2-\zeta^2}{C_1^2}E(m)\right], \tag{16}$$

with

$$C_0^2 = 1 + 2\eta + \eta^2 + \zeta^2 + \sigma^2, \tag{17}$$

$$C_1^2 = 1 - 2\eta + \eta^2 + \zeta^2 + \sigma^2, \tag{18}$$

and the functions $K(m)$ and $E(m)$ being the first and second type of complete elliptic integrals, respectively, with m defined as:

$$m = \frac{4\eta}{C_0^2}. \tag{19}$$

It should be noted that Eqs. (15) and (16) can only be used in the local vortex ring coordinate system $x^{'}y^{'}z^{'}$. Let's consider a global coordinate system xyz, with its origin O located at the center of the rotor disc (at the wind turbine's stable upright position), the x-axis pointing vertically upwards, opposite to gravity, the y-axis pointing to the left when looking in the nominal downwind direction, and the z-axis pointing in the nominal (0°) downwind direction. To compute the velocity induced at a control point P, with coordinate $\mathbf{X}_P$ in the global coordinate system, a coordinate transformation needs to be applied. First, the global coordinate $\mathbf{X}_P$ is transformed into the local coordinate $\mathbf{X}_P^{'}$ as

$$\hat{\mathbf{X}}_P^{xyz} = \underbrace{\mathbf{M}_{roll}(\gamma)\mathbf{M}_{pitch}(\chi)\mathbf{M}_{yaw}(\beta)}_{\text{rotation transformation}} \underbrace{(\mathbf{X}_P^{xyz} - \mathbf{X}_{\hat{o}}^{xyz})}_{\text{translation transformation}}, \tag{20}$$

where $\mathbf{X}_P^{xyz} = (x_P, y_P, z_P)$ is the coordinate of P in the original coordinate frame, $\hat{\mathbf{X}}_P^{xyz} = (\hat{x}_P, \hat{y}_P, \hat{z}_P)$ is the coordinate of P in the target coordinate frame, and $\mathbf{X}_{\hat{o}}^{xyz} = (x_{\hat{o}}, y_{\hat{o}}, z_{\hat{o}})$ is the coordinate of the origin of the target coordinate frame $\hat{O}$ in the original coordinate frame. Generally speaking, γ, χ and β are the roll, pitch and yaw angles, respectively, for the rotation transformation. The matrices $\mathbf{M}_{pitch}(\chi)$, $\mathbf{M}_{yaw}(\beta)$ and $\mathbf{M}_{roll}(\gamma)$ for rotation transformation in pitch, yaw and roll are given as

$$\mathbf{M}_{pitch}(\chi) = \begin{bmatrix} \cos\chi & 0 & \sin\chi \\ 0 & 1 & 0 \\ -\sin\chi & 0 & \cos\chi \end{bmatrix}, \quad \mathbf{M}_{yaw}(\beta) = \begin{bmatrix} 1 & 0 & 0 \\ 0 & \cos\beta & -\sin\beta \\ 0 & \sin\beta & \cos\beta \end{bmatrix}, \quad \mathbf{M}_{roll}(\gamma) = \begin{bmatrix} \cos\gamma & -\sin\gamma & 0 \\ \sin\gamma & \cos\gamma & 0 \\ 0 & 0 & 1 \end{bmatrix}. \tag{21}$$

The induced velocity calculated in the local frame of reference then needs to be transferred back to the global frame as

$$\mathbf{V}_P^{xyz} = \mathbf{M}_{yaw}^{-1}(\beta)\mathbf{M}_{pitch}^{-1}(\chi)\mathbf{M}_{roll}^{-1}(\gamma)\hat{\mathbf{V}}_P^{xyz}. \tag{22}$$

3. Numerical Model

As explained in Section 2, the present free wake vortex ring model consists of two parts: the near wake model and the far wake model. The near wake model includes the blade bound vortex model and the trailed vortex model, which are both represented by vortex line segments. The velocities induced by these vortex lines are calculated based on Biot-Savart's law as described in Section 2.1. By contrast, the velocity induced by the far wake model is given by Eqs. (15) and (16). Section 3.1 gives more insights into the discretisation of blades using vortex elements, while Section 3.2 discusses how the far wake model is implemented and how vortex rings propagate in the wake.

3.1. Near wake models

3.1.1. Blade bound vortex model

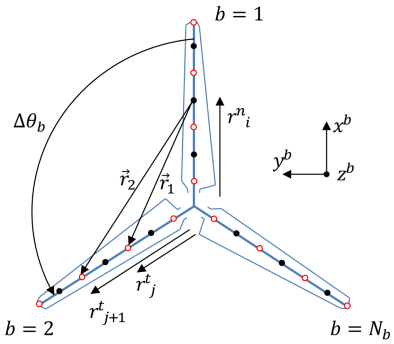

Figure 2. The blade bound vortex model

Figure 2 illustrates the blade bound vortex model for a rotor of $N_b = 3$ blades. Each blade is discretised with a series of vortex line segments. The radial endpoints of each vortex segment are marked by red hollow points and denoted by r_j^t and r_{j+1}^t respectively. The control points of each vortex line segment are marked by black solid dots denoted by r_i^n, where $r_i^n = (r_j^t + r_{j+1}^t)/2$ ($i = 1, ..., N$ and $j = 1, ..., N+1$), N being the number of vortex segments. A local blade coordinate system $x^b y^b z^b$ is defined. It is right-handed and centered at the rotor root. The x^b-axis is along the pitch axis and points towards the tip of the blade, the y^b-axis points to the trailing edge of blade and is parallel to the chord line at the zero-twist blade section, and the z^b-axis is orthogonal to both x^b and y^b. In the local blade coordinate system of a blade b, the rotor lies in the $x^b y^b$-plane as shown in Figure 2. The coordinates of a control point n_i and an endpoint t_j are then expressed as

$$\mathbf{n}_i = \begin{Bmatrix} 0 \\ r_i^n \\ 0 \end{Bmatrix}, \qquad \mathbf{t}_j = \begin{bmatrix} \cos\Delta\theta_b & -\sin\Delta\theta_b & 0 \\ \sin\Delta\theta_b & \cos\Delta\theta_b & 0 \\ 0 & 0 & 1 \end{bmatrix} \begin{Bmatrix} 0 \\ r_j^t \\ 0 \end{Bmatrix}, \tag{23}$$

where $\Delta\theta_b = (bi - b)2\pi/N_b$ is the angle between blade bi and blade b. Assuming $\mathbf{x}_P = \mathbf{n}_i, \mathbf{x}_1 = \mathbf{t}_1$ and $\mathbf{x}_2 = \mathbf{t}_2$, and substituting Eq. (23) into Eq. (7), it can be found that the velocity induced by the segment x_1x_2 at the control point $\mathbf{n}_i$ equals zero in both the x_b-direction and the y_b-direction, and in the z_b-direction is equal to

$$V_{ij}^{zb} = \Gamma_j^b \frac{r_i^n \sin\Delta\theta_b \left[r_2(r_j^t - r_i^n\cos\Delta\theta_b) - r_1(r_{j+1}^t - r_i^n\cos\Delta\theta_b) \right]}{4\pi r_1 r_2 \left[r_c^2 + r_i^{n2} - (r_i^n\cos\Delta\theta_b)^2 \right]} = A_{ij}^b \Gamma_j^b, \tag{24}$$

where A_{ij}^b is the influence coefficient which only depends on the geometry and discretization of the rotor, and r_1 and r_2 are the lengths of the vectors $\mathbf{x}_1 - \mathbf{x}_P$ and $\mathbf{x}_2 - \mathbf{x}_P$ respectively, i.e.

$$r_1 = \sqrt{r_c^2 + r_i^{n2} + r_j^{t2} - 2r_i^n\cos\Delta\theta_b}, \tag{25}$$

$$r_2 = \sqrt{r_c^2 + r_i^{n2} + r_{j+1}^{t\,2} - 2r_i^n\cos\Delta\theta_b}. \tag{26}$$

The total induced velocity at a control point n_i is the sum of the influences of all the bound vortex segments on all N_b blades, which can be expressed as

$$V_i^{zb} = \sum_{b=1}^{N_b} \sum_{j=1}^{N} V_{ij}^{zb} = \sum_{b=1}^{N_b} \sum_{j=1}^{N} A_{ij}^{b} \Gamma_j^{b}. \tag{27}$$

Considering that the rotor is axis-symmetric and that all the blades' geometry and discretization are identical, the total induced velocity at all N control points on a blade b, in the local blade coordinate system, can be simplified as

$$\left\{ V^{zb} \right\} = \sum_{b=1}^{N_b} \mathbf{A}^{b} \left\{ \Gamma^{b} \right\}, \tag{28}$$

where $\mathbf{A}^b$ is the matrix of influence coefficients of the blade bound vortex model.

3.1.2. Trailed vortex model

In this section, a finite length vortex line model is introduced as opposed to the semi-infinite vortex line model proposed by de Vaal[14], as shown in Figure 3a. A local blade coordinate system $x^b y^b z^b$ is used, where the rotor lies in the $x^b y^b$-plane and the blade b lies along the x^b-axis. In the present model, the trailed vortex line begins from an endpoint of a blade segment on the rotor and extends to a finite length l_j^t in the direction normal to the blade in the $x^b y^b$-plane. The length of a trailing vortex segment is defined as

$$l_j^t = r_j^t \theta_t, \tag{29}$$

which equals to the arc length of r_j^t times the angle θ_t swept, where θ_t is an input parameter.
The induced velocity at the control point n_i on blade b can be determined using Eq. (7). The coordinates of $\mathbf{x}_P$ and $\mathbf{x}_1$ are both given by Eq. (23), while the coordinates of $\mathbf{x}_2$ can be written as

$$\mathbf{x}_2 = \begin{bmatrix} \cos\Delta\theta_b & -\sin\Delta\theta_b & 0 \\ \sin\Delta\theta_b & \cos\Delta\theta_b & 0 \\ 0 & 0 & 1 \end{bmatrix} \begin{Bmatrix} r_j^t \theta_1 \\ r_j^t \\ 0 \end{Bmatrix}. \tag{30}$$

Substituting Eq. (23) and Eq. (30) into Eq. (7), evaluating the integral and simplifying, it is found that the induced velocity of a trailed vortex segment $x_1 x_2$ at a control point $\mathbf{n}_i$ in the x_b-direction and the y_b-direction are both zero, and that in z_b-direction, it is equal to

$$V_{ij}^{zt} = \Delta\Gamma_j^t \frac{(r_j^t - r_i^n \cos\Delta\theta_b)\left[r_2' r_i^n \sin\Delta\theta_b - r_1 (r_j^t - r_i^n \sin\Delta\theta_b)\right]}{4\pi r_1 r_2' \left[r_c^2 + r_j^{t\,2} - 2 r_i^n r_j^t \cos\Delta\theta_b - (r_i^n \cos\Delta\theta_b)^2\right]} = A_{ij}^t \Delta\Gamma_j^t, \tag{31}$$

where r_1 and r_2' are the lengths of the vectors $\mathbf{x}_1 - \mathbf{x}_P$ and $\mathbf{x}_2 - \mathbf{x}_P$, respectively, r_1 is as given in Eq. (25) and r_2' can be defined as

$$r_2' = \sqrt{r_c^2 + r_i^{n\,2} + r_j^{t\,2}(1 + \theta_1^2) - 2 r_i^n r_j^t (\cos\Delta\theta_b + \theta_1 \sin\Delta\theta_b)}. \tag{32}$$

The total velocity induced by the trailed vortex at a control point n_i is the sum of the influences of all the trailing vortex segments on all N_b blades, which can be expressed as

Preprints (www.preprints.org) | NOT PEER-REVIEWED | Posted: 6 August 2019 doi:10.20944/preprints201908.0078.v1

Peer-reviewed version available at Energies 2019, 12, 3900; doi:10.3390/en12203900

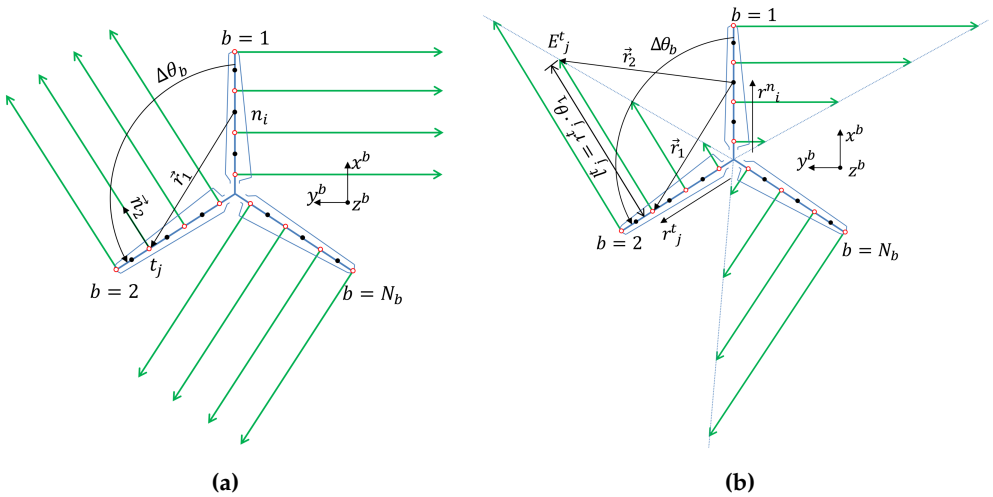

Figure 3. The trailed vortex models: infinite length (left), finite length (right).

$$V_i^{zt} = \sum_{b=1}^{N_b} \sum_{j=1}^{N+1} V_{ij}^{zt} = \sum_{b=1}^{N_b} \sum_{j=1}^{N+1} A_{ij}^t \Delta\Gamma_j^t. \tag{33}$$

Where $N+1$ is the number of trailing vortex segments. In the local blade coordinate system of blade b, the total velocity induced by the trailed vorticity at all N control points on blade b can thus be written as

$$\left\{V^{zt}\right\} = \sum_{b=1}^{N_b} \mathbf{A}^t \left\{\Delta\Gamma^t\right\}, \tag{34}$$

where $\mathbf{A}^t$ is the matrix of influence coefficients of the trailed vortex model.

3.1.3. Total induced velocity of the near wake

The total induced velocity of the near wake on a rotor blade is the sum of the components of the blade bound vortex model given by Eq. (28) and the components of the trailed vortex model given by Eq. (34). Considering that both components have non-zero values only in the z_b-direction, the z_b-component of the near wake induced velocity V^{nw} on the rotor blade is written as

$$V^{nw} = \sum_{b=1}^{N_b} \left(\mathbf{A}^b \left\{\Gamma^b\right\} + \mathbf{A}^t \left\{\Delta\Gamma^t\right\}\right). \tag{35}$$

It can be seen that the near wake induced velocities only depend on the rotor geometry and the distribution of the control points.

3.2. Far wake model

The far wake model is formulated based on the assumption that the spiral vortices in the wake of a wind turbine can be simplified into a series of vortex rings, as illustrated in Figure 4. When each of the N_b blades of the wind turbine sweeps $2\pi/N_b$ degrees, that is to say, when all the N_b blades of the wind turbine together sweep a full rotor revolution, a pair of new vortex rings R^1 is shed into the wake, the outer ring being shed from the outboard part of the rotor and the inner ring being shed from the inboard part of the rotor disc. The computation of the far wake induced velocity $\mathbf{V}_P^{fw}$ at a point

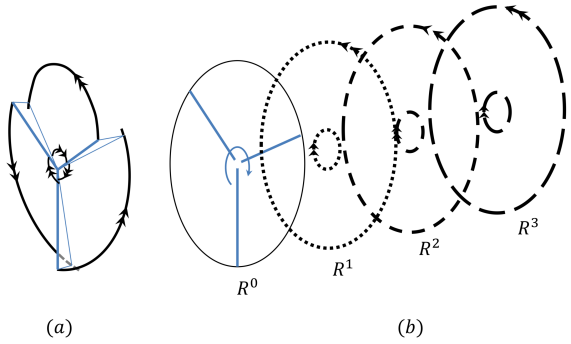

Figure 4. Schematic representation of a four vortex rings shed by the far wake model.

P in the global coordinate system is described in Section 2.2. With the contribution of all N_R pairs of vortex rings, it can be expressed as

$$\mathbf{V}_P^{fw} = \sum_{k=1}^{N_R} \mathbf{V}_{in,k} + \sum_{k=1}^{N_R} \mathbf{V}_{out,k}, \tag{36}$$

where $\mathbf{V}_{in,k}$ is the velocity induced by the k^{th} inner ring and $\mathbf{V}_{out,k}$ is that induced by the k^{th} outer ring. The induced velocity at the control point of the rotor can be used to determine the thrust, torque, and other aerodynamic parameters of the wind turbine, while the induced velocity at the control point on the vortex rings is used to determine the convection of the wake.

3.2.1. The propagation of vortex ring

All the existing vortex rings in the wake convect independently downstream as time evolves. Unlike the near wake model, which only depends on the geometry of the rotor, the far wake model is time-dependent. Two time scales are considered: (i) the time step for the vortex shedding defined as $\Delta T = T_P/N_b$, where T_P is the period of rotation of the rotor, and (ii) the time step used to compute the propagation of the vortex rings and defined as $\Delta t = \Delta T/n_{cst}$, where n_{cst} is a constant integer. The calculation of the propagation of vortex rings is a cyclic process which involves three steps per Δt at a time t.

1. Identify the control points on the vortex rings and calculate the velocities (including induced velocity and free stream velocity) on all the control points in the field.
2. Calculate the position of the control points both on the rotor and in the wake. The position of the control points on the rotor is determined by the position of the rotor and the azimuthal angle of the blade. The displacement of the control point in the wake is given by Euler's equation assuming an incompressible and inviscid fluid, as

$$\mathbf{S}(t + \Delta t) = \mathbf{S}(t) + \mathbf{V}\Delta t, \tag{37}$$

   where V is the speed of a control point in the global coordinate system.
3. Update the position of the vortex rings based on the position of the control points determined in step 2.

According to the geometry characteristics of a ring, a group of geometry parameters that completely describe a vortex ring k are collected into the variable $\mathbf{S}_k$, as

$$\mathbf{S}_k = \begin{Bmatrix} x_{O,k} \\ y_{O,k} \\ z_{O,k} \\ R_k \\ \chi_k \\ \beta_k \\ \gamma_k \end{Bmatrix} \quad k = 1, ..., N_R, \tag{38}$$

where the coordinates of the vortex ring center $\mathbf{O}_k = (x_{O,k}, y_{O,k}, z_{O,k})$, R_k is the ring radius, γ_k, χ_k and β_k namely roll, pitch and yaw angles are as defined in Section 2.2. All these parameters value can change in time. Here we consider a local inertial coordinate system $\hat{x}\hat{y}\hat{z}$ by translating the global coordinate to make its origin coincide with that of the vortex ring k without rotation. At the upright position, when the ring lies in the $\hat{x}\hat{y}$-plane, χ_k and β_k are both zero, and when it rotates anti-clockwise around the corresponding axis according to the right-hand law, the value of the angle is defined as positive. Due to the rotational invariance property of the vortex ring, the roll angle γ_k around the $\hat{z}$-axis has no influence on the position of the ring itself but represents the azimuthal angle between the ring and the control point. In the following part of this section, the method to determine these parameters is introduced.

Let's define a local vortex ring coordinate system $x^{'}y^{'}z^{'}$ by giving the local inertial coordinate system $\hat{x}\hat{y}\hat{z}$ a pitch angle of χ_k and then a yaw angle of β_k, so that the vortex ring lies in the $x^{'}y^{'}$-plane. During the numerical process, a vortex ring in the wake is represented by a series of control points distributed uniformly on the ring along the azimuthal angle $\Delta\theta$, as shown in Figure 5. For convenience, each control point is assigned a number, moving anti-clockwise from the first point $n = 1$ on the positive $y^{'}$-axis to the last point $n = N_c$. With a total of N_c control points on a vortex ring, $\Delta\theta = 2\pi/N_c$. Thus the coordinate $\mathbf{X}^{'}_{i,k} = (x^{'}_{i,k}, y^{'}_{i,k}, z^{'}_{i,k})$ of a control point i on a vortex ring k in the local vortex ring coordinate system is given by

$$\begin{cases} x^{'}_{i,k} = R_k \sin[\Delta\theta(i-1)] \\ y^{'}_{i,k} = R_k \cos[\Delta\theta(i-1)] \\ z^{'}_{i,k} = 0 \end{cases} \quad i = 1, ..., N_c, k = 1, ..., N_R. \tag{39}$$

These local coordinates need to be expressed in the global coordinate system denoted by $\mathbf{X}_{i,k}(t - \Delta t)$

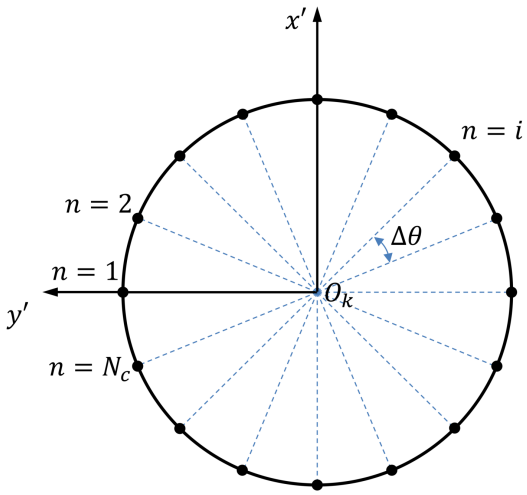

Figure 5. Control points on vortex ring

as explained in Section 2.2. At each time step t , the control point velocity $V_{i,k}$ is updated according to

Peer-reviewed version available at Energies 2019, 12, 3900; doi:10.3390/en12203900

the development of the wake. The new position of the control point denoted by $\mathbf{X}_{i,k}(t)$ is determined by Eq. (37) as:

$$\mathbf{X}_{i,k}(t) = \mathbf{X}_{i,k}(t - \Delta t) + \mathbf{V}_{i,k}\Delta t. \tag{40}$$

Since the control points move independently, the new positions of the control points may no longer form an exact circle. This discrepancy is however very small if the time step Δt is small enough. Nevertheless, a new vortex ring with the geometry parameters as shown in Eq. (38) needs to be determined by the updated position of the azimuthal control points. Firstly, the vortex ring origin coordinate $\mathbf{O}_k$ can be expressed by taking the average of the coordinates of all the control points as

$$\mathbf{O}_k = \frac{1}{N_c}\sum_{i=1}^{N_c}\mathbf{X}_{i,k} = \frac{1}{N_c}\sum_{i=1}^{N_c}(x_{i,k}, y_{i,k}, z_{i,k}). \tag{41}$$

Next, the vortex ring radius R_k are determined by taking the average of the length of the segment $\mathbf{s}_{i,O}$ from each control point i to the center of the ring $\mathbf{O}_k$ as

$$R_k = \frac{1}{N_c}\sum_{i=1}^{N_c}\sqrt{(x_{i,k} - x_{O,k})^2 + (y_{i,k} - y_{O,k})^2 + (z_{i,k} - z_{O,k})^2}. \tag{42}$$

In order to determine the pitch angle χ_k and yaw angle β_k of the vortex ring k, a so-called average midline method is proposed. In this method, the rotational angles of the midlines of the ring ($x^{'}$-axis for pitch and $y^{'}$-axis for yaw in the local vortex ring coordinate frame respectively) in the global reference frame are taken as the rotational angles of the vortex ring as indicated in Figure 6. Since the control points should be symmetric with respect to the midline axis of the ring, the coordinates of the control points on both sides of the midline are summed up to represent the coordinate of a point on the midline. To avoid obtaining a zero summation, the coordinates of the control points are summed up on the positive axis of the midline and the negative axis of the midline, respectively, and the angles are calculated separately. An average is then used as the final value. For this method to be accurate, the number of control points N_c should be even. The expressions are given by

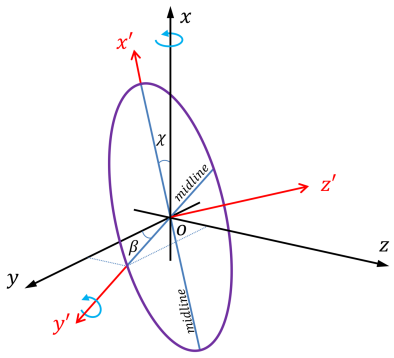

Figure 6. Schematic representation of the coordinate system and ring for the average midline method.

$$\begin{aligned}\chi_k &= -\frac{1}{2}(\arctan\frac{dz_1}{dx_1} + \arctan\frac{dz_2}{dx_2}),\\ \beta_k &= \frac{1}{2}(\arctan\frac{dz_3}{dy_1} + \arctan\frac{dz_4}{dy_2}),\end{aligned} \tag{43}$$

where dx_1,dx_2,dy_1,dy_2, dz_1,dz_2,dz_3 and dz_4 are defined as

$$
\begin{aligned}
dx_1 &= \sum_{x'_{i,k}>=0} x'_{i,k}, \quad dz_1 = \sum_{x'_{i,k}>=0} z'_{i,k}, \\
dx_2 &= \sum_{x'_{i,k}<0} x'_{i,k}, \quad dz_2 = \sum_{x'_{i,k}<0} z'_{i,k}, \\
dy_1 &= \sum_{y'_{i,k}>=0} y'_{i,k}, \quad dz_3 = \sum_{y'_{i,k}>=0} z'_{i,k}, \\
dy_2 &= \sum_{y'_{i,k}<0} y'_{i,k}, \quad dz_4 = \sum_{y'_{i,k}<0} z'_{i,k}.
\end{aligned} \tag{44}
$$

3.3. Characteristics of the first rings shed in the wake

After a certain distance behind the rotor, the trailed vortex segments of the near wake roll up into two concentrated vortex rings in the far wake, namely the outer vortex ring and the inner vortex ring, as discussed in Section 3.2. The initial size and vortex strength of the vortex rings are defined in this section. The algorithms of the roll-up process is based on the momentum conservation theory [18], as applied by de Vaal [14]. The location of the maximum blade bound vortex strength Γ_{max} is used to distinguish between inner and outer rings. In particular, the near wake trailing vortices between the location of Γ_{max} and the tip of the blade are roll up into an outer ring and the near wake trailing vortices between the location of Γ_{max} and the root of the blade roll up into an inner ring in the far wake. The vortex strengths of the roll up vortex ring must be equal to the summation of the vortex strengths of the trailing vortices from which it is formed. Generally speaking, the vortex strength $\bar{\Gamma}$ and radius $\bar{r}$ of a vortex ring formed by the vortices trailed between blade radius r_1 and r_2 is given by

$$
\bar{\Gamma} = -\int_{r_1}^{r_2} \frac{d\Gamma}{dr} dr, \tag{45}
$$

$$
\bar{r} = \frac{1}{\bar{\Gamma}} \int_{r_1}^{r_2} r \frac{d\Gamma}{dr} dr. \tag{46}
$$

These equations can be used to get the expression for the inner and outer concentrated vortex strengths $\bar{\Gamma}^b_{in}$ and $\bar{\Gamma}^b_{out}$ and vortex ring radii $\bar{r}^b_{in}$ and $\bar{r}^b_{out}$ independently on each blade b, i.e.

$$
\bar{\Gamma}^b_{in} = -\int_{r_1}^{r_2} \frac{d\Gamma^b}{dr} dr = \sum_{n=1}^{n_{max}} \Delta\Gamma^t_n, \tag{47}
$$

$$
\bar{r}^b_{in} = \frac{1}{\bar{\Gamma}^b_{in}} \int_{r_1}^{r_2} r \frac{d\Gamma^b}{dr} dr = \frac{1}{\bar{\Gamma}^b_{in}} \sum_{n=1}^{n_{max}} r_n \Delta\Gamma^t_n, \tag{48}
$$

$$
\bar{\Gamma}^b_{out} = -\int_{r_1}^{r_2} \frac{d\Gamma^b}{dr} dr = \sum_{n=n_{max}+1}^{N+1} \Delta\Gamma^t_n, \tag{49}
$$

$$
\bar{r}^b_{out} = \frac{1}{\bar{\Gamma}^b_{out}} \int_{r_1}^{r_2} r \frac{d\Gamma^b}{dr} dr = \frac{1}{\bar{\Gamma}^b_{out}} \sum_{n=n_{max}+1}^{N+1} r_n \Delta\Gamma^t_n. \tag{50}
$$

Since each of the blade contributes equally to the far wake vortex ring, the final concentrated vortex strength and radius of the inner and outer ring for the whole rotor are defined as an average of the concentrated vortex strengths and radii calculated from each of the blades, that is

$$
\bar{\Gamma}_{out} = \frac{1}{N_b} \sum_{b=1}^{N_b} \bar{r}^b_{out}, \qquad \bar{\Gamma}_{in} = \frac{1}{N_b} \sum_{b=1}^{N_b} \bar{r}^b_{in}, \tag{51}
$$

$$\bar{r}_{out} = \frac{1}{N_b}\sum_{b=1}^{N_b} \bar{r}^b_{out}\,, \qquad \bar{r}_{in} = \frac{1}{N_b}\sum_{b=1}^{N_b} \bar{r}^b_{in}. \tag{52}$$

3.4. Strength of the blade bound vortex

Based on the discussion above, it can be seen that both the trailing vortex strengths and the far wake vortex ring strengths are determined by the distribution of blade bound vortex strengths. Once the blade bound vortex strengths are known, the near wake induced velocity at any point of the rotor can be determined by Eq. (35) and the far wake vortex ring strengths are determined at the roll-up processes and with no change during their convection in the wake. Thus the blade bound vortex strengths need to be determined as a prerequisite. A method to calculate the blade bound vortex strengths based on the three-dimensional vortex lifting law and the blade element theory is discussed below.

3.4.1. Three-dimensional vortex lifting law

The three-dimensional vortex lifting law as introduced by Phillips [19] is adopted to solve the blade bound vortex strength. Based on this theory, the lift force $d\mathbf{F}_l$ acting on a vortex segment $d\mathbf{l}$ can be calculated by the product of the air density ρ, the bound vortex strength Γ^b on the segment, and the relative wind velocity $\mathbf{V}$, as

$$d\mathbf{F}_l = \rho\Gamma^b\mathbf{V}\times d\mathbf{l}, \tag{53}$$

where the relative wind velocity $\mathbf{V}$ includes the contribution from the free stream $\mathbf{V}_\infty$, the rotor rotation $\mathbf{V}^\Omega$, the near wake induced velocity $\mathbf{V}^{nw}$, the far wake induced velocity $\mathbf{V}^{fw}$, as well as the contribution from the motion of the turbine $\mathbf{V}_p$ in the case of a floating offshore wind turbine. The relative wind velocity $\mathbf{V}$ can be further decomposed into three components in the blade coordinate system as V_{xb} in the x^b-direction, which is along the pitch axis towards the tip of the blade, and V_{yb} and V_{zb} lie in the blade section and are normal to the blade pitch axis. Thus the relative wind velocity $\mathbf{V}$ can be written as

$$\mathbf{V} = \mathbf{V}_\infty + \mathbf{V}^\Omega + \mathbf{V}^{nw} + \mathbf{V}^{fw} + \mathbf{V}_p = \begin{Bmatrix} V_{xb} \\ V_{yb} \\ V_{zb} \end{Bmatrix}, \tag{54}$$

where the velocity of a floating support structure $\mathbf{V}_p$ is determined as [20]

$$\begin{aligned} \mathbf{V}_p &= \dot{\mathbf{x}}_p + \dot{\theta}_p \times \mathbf{x}_p \\ &= \begin{Bmatrix} x_{heave} \\ -y_{sway} \\ z_{surge} \end{Bmatrix} + \begin{Bmatrix} \dot{\theta}_{yaw} \\ -\dot{\theta}_{pitch} \\ \dot{\theta}_{roll} \end{Bmatrix} \times \begin{Bmatrix} x \\ y \\ z \end{Bmatrix} \\ &= \begin{Bmatrix} \dot{x}_{heave} + z\dot{\theta}_{pitch} - y\dot{\theta}_{roll} \\ -\dot{y}_{sway} + x\dot{\theta}_{roll} - z\dot{\theta}_{yaw} \\ \dot{z}_{surge} + x\dot{\theta}_{pitch} + y\dot{\theta}_{yaw} \end{Bmatrix}. \end{aligned} \tag{55}$$

Substituting Eq. (54) into (53), and given that the x^b-axis is parallel to $d\mathbf{l}$, it is found that only the V_{yb} and V_{zb} components contribute to the lifting force acting on the blade. Thus Eq. (53) can be rewritten as

$$d\mathbf{F}_l = \rho\Gamma^b\mathbf{V}^n\times d\mathbf{l}, \tag{56}$$

where $\mathbf{V}^n$ is the velocity vector that has only the V_{yb} and V_{zb} components, i.e.

$$\mathbf{V}^n = \begin{Bmatrix} 0 \\ V_{yb} \\ V_{zb} \end{Bmatrix}. \tag{57}$$

3.4.2. Blade element force

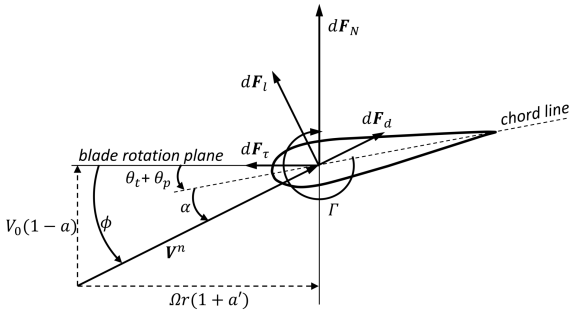

Figure 7. Forces acting on a blade element.

The lift force on a blade segment can also be calculated from the airfoil properties of the segment as indicated in Figure 7. The lift force can be expressed as

$$d\mathbf{F}_l = \frac{1}{2}\rho \left|\mathbf{V}^n\right|^2 C_l c dl, \tag{58}$$

where $\mathbf{V}_n$ is defined in Eq. (57), c is the chord length of the blade section, and C_l is the lift coefficient which can be obtained by means of tabulated aerodynamic parameters of the airfoil with a given angle of attack α. The angle of attack can be calculated with the fluid velocity around the blade section as

$$\alpha = \phi - (\theta_t + \theta_p), \tag{59}$$

where θ_t is the twist angle of the blade section , θ_p is the collective pitch angle of the blade and the angle of relative wind ϕ is the angle between the wind velocity $\mathbf{V}_n$ and the plane of the rotor disc, which can be expressed as

$$\phi = tan^{-1}\frac{V_0(1-a)}{\Omega r(1+a')}. \tag{60}$$

In Eq. (60), Ω is the rotor angular speed, a is the axial induction factor and a' is the angular induction factor. Similar to the lift force, the drag force $d\mathbf{F}_d$ can be calculated from the tabulated drag coefficient C_d and the angle of attack α, leading to

$$d\mathbf{F}_d = \frac{1}{2}\rho \left|\mathbf{V}^n\right|^2 C_d c dl. \tag{61}$$

Based on the discussion above, it is found that both Eq. (56) and Eq. (58) express the lift force of the blade segment. Thus by equating them for a blade section i, the following relation is obtained

$$\Gamma_i^b |\mathbf{V}_i^n(\Gamma_j) \times d\mathbf{l}_i| - \frac{1}{2}|\mathbf{V}_i^n(\Gamma_j)|^2 C_l(\alpha_i) c_i dl_i = 0. \tag{62}$$

For each blade section $i = 1, ..., (N_b \cdot N)$, an equation like Eq. (62) can be set up. For all $(N_b \cdot N)$ blade sections, a system of $(N_b \cdot N)$ non-linear equations are obtained and solved for $(N_b \cdot N)$ unknown values of the bound vortex strength Γ_i^b. Different methods can be used to solve the resulting set of non-linear equations. The trust-region methods are used here they proved to be more stable and

Peer-reviewed version available at Energies 2019, 12, 3900; doi:10.3390/en12203900

converge more rapidly than Newton-Raphson methods, especially for small and negative angles of attack. Accordingly, the rotor thrust $\mathbf{F}_T$ is expressed as

$$\mathbf{F}_T = \sum_{b=1}^{N_b} \sum_{j=1}^{N} d\mathbf{F}_N = \sum_{b=1}^{N_b} \sum_{j=1}^{N} d\mathbf{F}_l \cos\phi + d\mathbf{F}_d \sin\phi, \tag{63}$$

whilst the torque Q is given by

$$Q = \sum_{b=1}^{N_b} \sum_{j=1}^{N} d\mathbf{F}_T r = \sum_{b=1}^{N_b} \sum_{j=1}^{N} (d\mathbf{F}_l \sin\phi - d\mathbf{F}_d \cos\phi) r. \tag{64}$$

4. Simulation description

This simplified free wake vortex model aims at finding a compromise between physical accuracy and low computational cost. In this section, we compare the computational cost of the present method with other methods available in the literature. Table 1 shows the methods under consideration with computational cost and modeling capability: blade element momentum theory (BEM), actuator disc with free wake vortex ring model (AFWRV) of de Vaal[10] and Yu[11], the present free wake vortex ring model (FWVR), and two more advanced vortex methods- the free wake vortex filament (FWVF) method of Sebastian[5] and the nonlinear vortex lattice method (NVLM) method of Lee [6].

Table 1. Computational time and function of different models.

Method	Computational time	Modeling capability
BEM	$C_b N_\theta N_\Omega$	Rotor aerodynamics without wake
AFWVR	$\frac{1}{3} C_a N_b^2 N_\theta^2 N_\Omega^3$	Rotor aerodynamics, uncoupled wake aerodynamics
FWVR	$\frac{1}{3} C_r N_b^2 N_\theta^2 N_\Omega^3 + C_\Gamma N_\theta N_\Omega$	Coupled rotor aerodynamics and wake aerodynamics
FWVF	$\frac{1}{3} C_f N_b^2 N_\theta^3 N_\Omega^3 + C_\Gamma N_\theta N_\Omega$	Coupled rotor aerodynamics and wake aerodynamics
NVLM	$\frac{1}{3} C_m N_b^2 N_\theta^3 N_\Omega^3 + C_\Gamma N_\theta N_\Omega$	Coupled rotor aerodynamics and wake aerodynamics

In this table, N_b is the number of rotor blades, N_θ is the number of time steps per rotor rotation and N_Ω is the number of rotor rotation to be simulated. $N_\theta N_\Omega$ represents the total number of time steps. C_b represents the time cost of evaluating the induced velocity at a point in the field with BEM, C_a, C_r, C_f and C_m represent the time cost of evaluating the induced velocity of a vortex element (vortex rings or vortex filaments) at a point in the field with AFWVR, FWVR, FWVF and NVLM respectively. Whether the blades are modeled or not, all the four methods are evaluated with the same number of control points on the rotor and with the same number of time steps.

The BEM theory method solves the induced velocities on the rotor based on the momentum theory and the blade element theory. The number of control points are constant and each point is considered independently. Thus the computational time has a linear relationship with the number of time steps, which is the fastest method for aerodynamic simulations. C_b involves the iterative solution of BEM equations and some analytical corrections, such as Prandtl tip-loss, Prandtl hub-loss, and Pitt and Peters skewed-wake corrections when needed.

By contrast, the solution of the other four vortex methods mainly includes two parts: the calculation of the vortex element strength and the calculation of the induced velocity including self-induced velocity and mutually induced velocity. The induced velocities are solved on the rotor as well as in the wake. The number of points where the induced velocities need to be calculated increases with the number of vortex elements in the wake (being vortex rings or vortex filaments) and each control point is induced by all the vortex elements in the field.

The vortex ring strength of AFWVR is directly determined from a prescribed thrust coefficient C_t[10], so the computational time is negligible. By contrast, the FWVR and FWVF methods first determine the blade bound vortex strength by iteratively solving the equations based on the 3D vortex lifting law and the blade element theory with tabulated data of lift coefficient C_l, and then the vortex strengths are distributed to the new generated vortex rings or vortex filaments in the wake. The computational times to determine the vortex strengths for FWVR, FWVF and NVLM methods at each time step are identical and denoted by C_Γ. Since C_Γ and C_b are both iterative processes with the same number of equations, they are considered to be of the same order of magnitude.

The computational times for evaluating the induced velocities of FWVR and FWVF are given in de Vaal[14] and van Garre[21]. Since the number of vortex filaments is N_θ times the number of vortex rings, the number of induced velocities that needs to be calculated at each time step for FWVR is also N_θ times that of FWVF. Since AFWVR has the same number of control points and vortex rings than FWVR, the number of induced velocities that needs to be calculated is the same. C_a involves the analytical solution of a vortex ring induced velocity, which includes the evaluation of the elliptic integrals of the first and second kind. C_r involves the same calculation as C_a as well as the analytical solutions of near wake induced velocities at the rotor points where the time cost is very small. Thus C_r is approximately equal to C_a. C_f involves the solving of the trigonometry functions based on Biot-Savart law, and C_m involves the solving of Biot-Savart kernel functions. Thus C_f and C_m are considered to be the same order of magnitude and slightly less expensive than C_r[14].

As expected, the above analysis shows that more physically accurate models are also more computationally expensive. BEM is the fastest model amongst those considered here. AFWVR and FWVR differ in solving the blade bound vortex strength equations, which is approximately the computational time of BEM, whilst FWVR, FWVF and NVLM differ in a factor N_θ for the computation of the induced velocities, which can be significant. Regarding the modeling capability, BEM evaluates the rotor aerodynamics without considering the wake aerodynamics. AFWVR evaluates both rotor and aerodynamics, but uses a prescribed thrust coefficient to determine the vortex strengths. This prevents further analysis on the influence of the wake on the rotor. FWVR, FWVF and NVLM evaluate the coupled rotor aerodynamics and the wake aerodynamics, thus presenting similar capabilities, despite the fact that FWVR discretizes the wake into vortex rings. Thus Table 1 shows that the present simplified numerical model has low computational cost and relatively high performance compared to other reference models.

5. Results

Results are shown for the NREL 5MW reference turbine, with rotor blades and tower assumed to be rigid. The basic parameters of the turbine are shown in Table 2, and the airfoils and aerodynamic properties distribution along the blade are given in Table 3. The rotor speed and blade pitch data corresponding to wind speeds from cut-in to cut-out are given in Figure 8. Other information can be found in the NREL report[22]. In this section, results are shown for three cases: bottom-mounted, floating restricted to one degree of freedom, and floating in three degrees of freedom.

5.1. Bottom-mounted wind turbine

In this section, a bottom-mounted wind turbine placed on a monopile support structure in a constant free stream is first considered to validate the present model. The rotor thrust F_T for wind speeds varying from the cut-in value of 3 m/s to the cut-out value of 25 m/s is shown in Figure 9. It is compared to different results from the literature, obtained under the same load cases, namely the results from NREL[22] that are calculated using FAST-Aerodyn based on the BEM theory, the results from Sørensen[**?**] where the Reynolds-averaged Navier–Stokes (RANS) method was used, and the results from Lee [6] that uses a nonlinear vortex lattice method (NVLM). Figure 9 shows that the present thrust results are close to those from NREL, especially for wind speeds between 6m/s and 15m/s, while the thrusts obtained from RANS and NVLM are consistently lower. For wind speeds

Table 2. Properties of NREL 5MW reference turbine.

Rating	**5MW**
Rotor Orientation, Configuration	Upwind, 3 Blades
Control	Variable Speed, Collective Pitch
Drivetrain	High Speed, Multiple-Stage Gearbox
Rotor, Hub Diameter	126 m, 3 m
Hub Height	90 m
Cut-In, Rated, Cut-Out Wind Speed	3 m/s, 11.4 m/s, 25 m/s
Cut-In, Rated Rotor Speed	6.9 rpm, 12.1 rpm
Rated Tip Speed	80 m/s
Overhang, Shaft Tilt, Precone	5 m, 5°, 2.5°

Table 3. Distributed blade aerodynamic properties of the NREL 5MW reference turbine.

Node (-)	RNodes (m)	AeroTwst (°)	DRNodes (m)	Chord (m)	Airfoil Table (-)
1	2.8667	13.308	2.7333	3.542	Cylinder1.dat
2	5.6000	13.308	2.7333	3.854	Cylinder1.dat
3	8.3333	13.308	2.7333	4.167	Cylinder2.dat
4	11.7500	13.308	4.1000	4.557	DU40_A17.dat
5	15.8500	11.480	4.1000	4.652	DU35_A17.dat
6	19.9500	10.162	4.1000	4.458	DU35_A17.dat
7	24.0500	9.011	4.1000	4.249	DU30_A17.dat
8	28.1500	7.795	4.1000	4.007	DU25_A17.dat
9	32.2500	6.544	4.1000	3.748	DU25_A17.dat
10	36.3500	5.361	4.1000	3.502	DU21_A17.dat
11	40.4500	4.188	4.1000	3.256	DU21_A17.dat
12	44.5500	3.125	4.1000	3.010	NACA64_A17.dat
13	48.6500	2.319	4.1000	2.764	NACA64_A17.dat
14	52.7500	1.526	4.1000	2.518	NACA64_A17.dat
15	56.1667	0.863	2.7333	2.313	NACA64_A17.dat
16	58.9000	0.370	2.7333	2.086	NACA64_A17.dat
17	61.6333	0.106	2.7333	1.419	NACA64_A17.dat

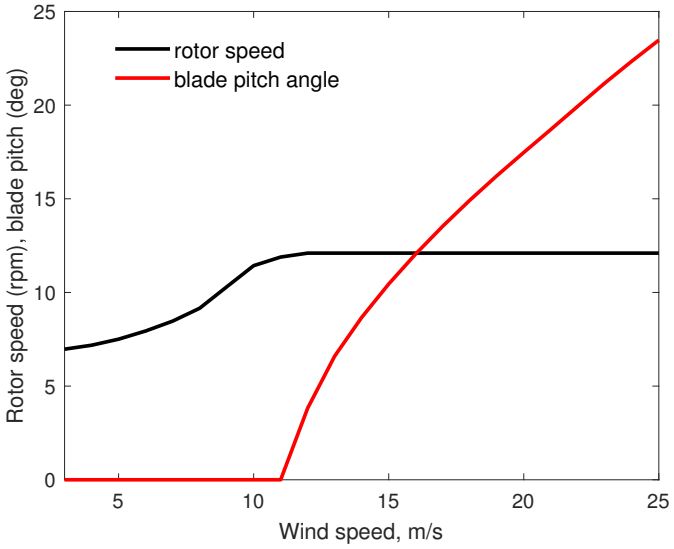

Figure 8. Rotor speed and blade pitch angle of NREL 5MW reference turbine.

smaller than 6m/s or higher than 15m/s, the thrust force computed by the present method starts to under-predict that from NREL. The comparison with RANS and NVLM is not available for wind speeds smaller than 6m/s. According to the literature, BEM is not accurate enough in low speed regions[23] and high speed regions where flow separation occurs[24]. These results suggest that the present vortex ring method can provide better results than BEM in low and high wind speed regions.

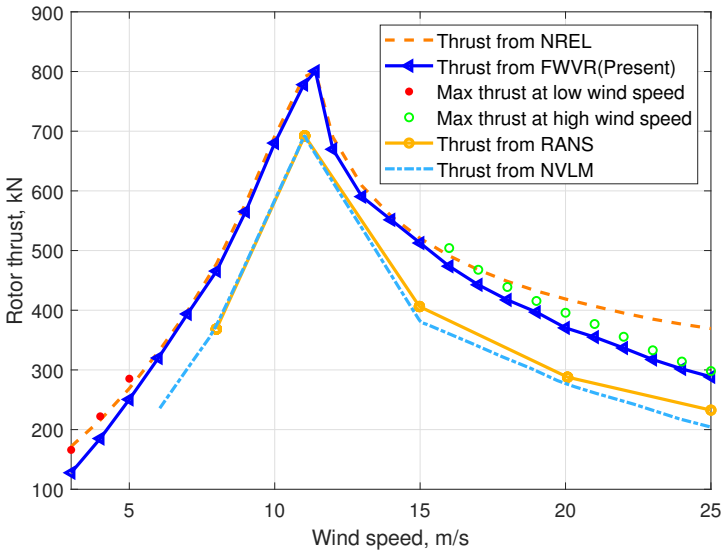

Figure 9. Comparison of the thrust force of monopile NREL 5MW wind turbine as a function of the wind speed.

In order to confirm this observation, an evaluation is made of the upper limit that the thrust force can theoretically achieve. As shown in Eq.(59), the angle of attack α is determined by the angle of relative wind ϕ minus the twist angle θ_t and the collective pitch angle θ_p. When θ_t and θ_p are together larger than ϕ, α is negative. As can be seen in Fig. 7, ϕ and α get the maximum value when a and a' are both zero. The maximum values of ϕ and α at different wind speeds are given in Fig. 10 and Fig. 11, respectively. In the low wind speed range (3m/s to 5 m/s), the values of α are between $0^\circ - 15^\circ$ in most parts of the blade. In this region, both the lift and drag coefficients of the airfoils are monotonically increasing (see Figures $3-1$ to $3-6$ in [22]). From Eq. (58) and Eq. (61), it can be deduced that when α is maximum, the lift and drag forces are also maximum and the values of ϕ are between 5° and 30°. Thus, following Eq. (63), the thrust force is maximum and the lift force dominates. The corresponding theoretical maximum values of the thrust force at low wind speeds are calculated and shown with red dots in Fig. 9.

In the high wind speed range (16m/s to 25 m/s), the values of α are between -5° and 30° in most parts of the blade. NREL's report[22] shows that when α is in the region $15^\circ - 30^\circ$, the lift coefficients fluctuate and the drag coefficients monotonically increase. Such angles of attack are encountered in the inboard part of the blade, where the corresponding ϕ are larger than 45°, which means the drag force dominates the value of thrust. And when α varies in the range -5° to 0°, the lift coefficients of the airfoils monotonically increase and the drag coefficients decrease. This region is on the outboard part of the blade, where the corresponding ϕ are smaller than 30°, which means that the lift force dominates the value of thrust. From the reasoning above, it is concluded that, in the high speed regions, the thrust force is maximum when α is maximum. The theoretical maximum values of thrust in the high wind speed region are calculated and shown with blue dots in Fig. 9.

Figure 9 shows that the thrust given by the free wake vortex ring method is consistently smaller than the theoretical maximum values, which is not the case of the thrust force given by the BEM theory. Thus, the thrust calculated with the free wake vortex ring method at low and high wind speeds is considered to be more reliable than that given by the BEM theory.

Preprints (www.preprints.org) | NOT PEER-REVIEWED | Posted: 6 August 2019 doi:10.20944/preprints201908.0078.v1

Peer-reviewed version available at Energies 2019, 12, 3900; doi:10.3390/en12203900

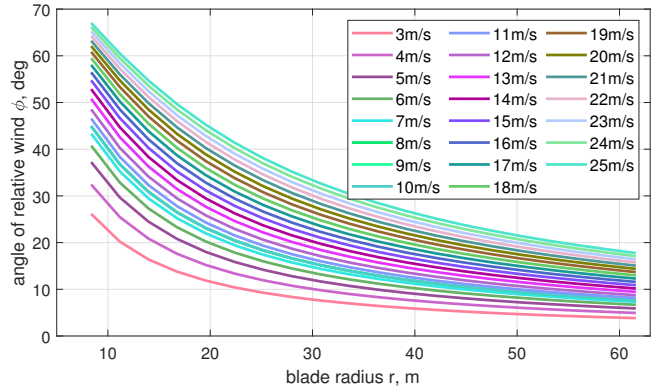

Figure 10. Maximum values of angle of relative wind ϕ.

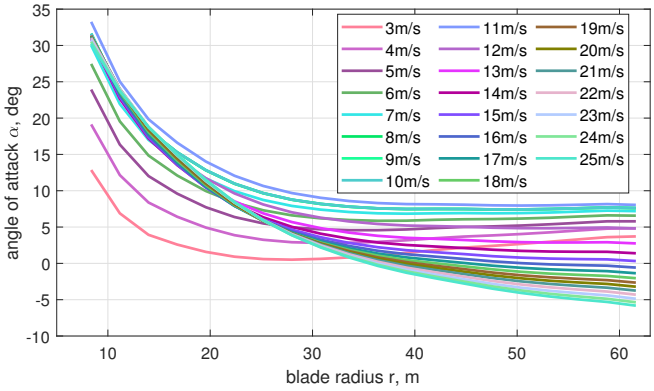

Figure 11. Maximum values of angle of attack α.

5.2. Floating wind turbine under single-DoF motion

Since the results from the present vortex ring method are shown to be reliable for a bottom-mounted wind turbine, the method is applied to a floating offshore wind turbine with a platform motion prescribed in one degree of freedom (DoF). The associated thrusts are compared with those of Lee [6] for the operating and environmental conditions presented in Table 4, a wind speed of 8 m/s, and a rotor speed of 9.16 rpm. The platform motions are prescribed as a sine function with motion amplitude (A) and frequency (f), as

$$X(t) = A_1 \sin(2\pi f_1 t). \tag{65}$$

Table 4. Amplitude and frequency of prescribed single-DoF motions[6]

Motion	Amplitude A [m or °]	Frequency f [Hz]
Translation (surge, sway, heave)	4	0.1
Rotation (roll, pitch, yaw)	4	0.05
surge	4,8,12	0.03
pitch	2,4,6	0.03

Figure 12 shows the results of thrusts with translational (surge, sway, heave, on Fig. 12a) and rotational (yaw, pitch, roll, on Fig. 12b) platform motions. The thrust force for a bottom-fixed wind turbine is also provided for comparison. It is found that the present FWVR method predicted an bottom fixed thrust of about 440 kN and the NVLM method predicted an bottom fixed thrust of about

Preprints (www.preprints.org) | NOT PEER-REVIEWED | Posted: 6 August 2019 doi:10.20944/preprints201908.0078.v1

Peer-reviewed version available at Energies 2019, 12, 3900; doi:10.3390/en12203900

380 KN, which are both consistent with the thrusts shown in Fig. 8 for these two methods. When the turbine is moving, the thrust forces obtained from both methods follow similar trends in both amplitude and frequency. Only the averaged value is slightly offset, which is in line with the offset observed for the bottom-mounted case. Figure 12a shows that, under translational platform motions, the thrust is most sensitive to surge, whilst Fig. 12b shows that, under roational platform motions, the thrust is most sensitive to pitch. This can be understood as these two motions are in line with the wind direction, and therefore, they influence the relative wind speed normal to the rotor disc. When the rotor has a leeward speed, the relative wind speeds are reduced on the blades and the angle of attacks are smaller, which leads to a lower thrust load than average. When the rotor has a windward speed, the situation is reverse and the thrust load is larger than average. It is also observed that the heave and sway motions of the same amplitude and frequency theoretically have equivalent influence to the rotor thrust. The heave and sway motions can change the relative tangential wind speed on the airfoils, which either increases or decreases the angle of attack according to the azimuthal angle of the blade, thus increasing or decreasing the thrust. However, this influence is relatively small as the change of tangential wind speed is much smaller than the tangential speed coming from the rotor rotation. From Figure 12a it can be seen that, with the present FWVR method, the thrust force under heave and sway motions almost overlap and slightly fluctuate around the thrust value of the bottom-mounted turbine, which is deemed to be reasonable.

The effect of the roll motion on the thrust is similar to that of the heave and sway motions, which mainly influence the relative tangential wind speed and the wake induced velocity on the rotor. The yaw motion can reduce the overall wind area of the rotor, hence reducing the thrust load compared to the bottom-mounted turbine, as obtained for both NVLM and FWVR.

The effect of the surge and pitch motions with different amplitudes are further analyzed and compared with the results of Lee [6] in Fig. 13. Figure 13a compares the thrust with surge motions with the amplitude of 4m, 8m, 12m and the frequency of 0.03Hz, whilst Fig. 13b compares the thrust with pitch motions with the amplitude of 2°, 4°, 6° and the frequency of 0.03Hz. As observed previously, the amplitudes and frequencies of the thrusts from NVLM and FWVR match well, whilst the offset in the mean values comes from the offset observed on the bottom-mounted turbine. Since the amplitudes of the platform motions are small and the frequency is relatively low, the amplitudes of the thrusts increase linearly with the increase in motion amplitudes for both surge and pitch.

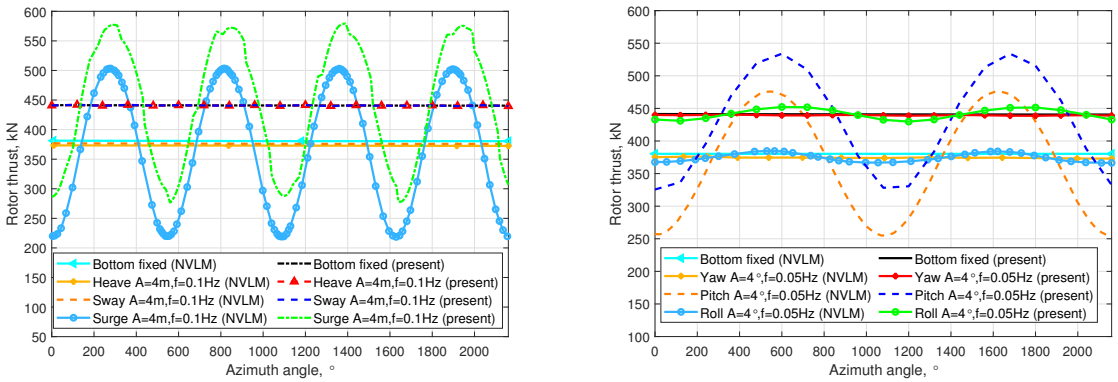

(a) **(b)**

Figure 12. Variation in the thrust of wind turbine in (a) translational motions (A=4m, f=0.1Hz) and (b) rotational motions (A=4°, f=0.05Hz).

Additional comparisons are made with the works of Sebastian [5] and de Vaal [14], for different floater types, under the following operating and environmental conditions:

1. below-rated: $V_\infty = 6.0m/s$,$\lambda = 9.63$,$H_s = 1.83m$,$T_p = 12.72s$,

Preprints (www.preprints.org) | NOT PEER-REVIEWED | Posted: 6 August 2019 doi:10.20944/preprints201908.0078.v1

Peer-reviewed version available at Energies 2019, 12, 3900; doi:10.3390/en12203900

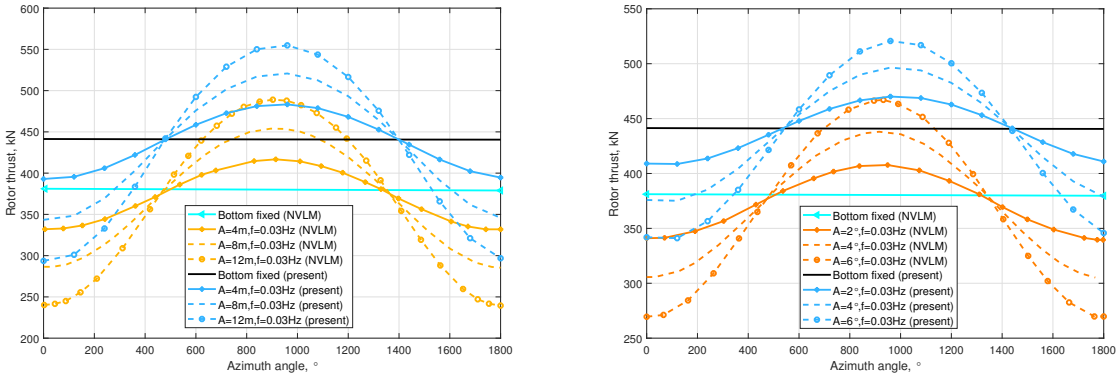

(a) **(b)**

Figure 13. Variation in the thrust of wind turbine in (a) surge (A=4m,8m,12m, f=0.03Hz) and (b) pitch (A=2°, 4°, 6°, f=0.03Hz).

2. rated: $V_\infty = 11.4m/s, \lambda = 7.00, H_s = 2.54m, T_p = 13.35s$, and
3. above-rated: $V_\infty = 18.0m/s, \lambda = 4.43, H_s = 4.09m, T_p = 15.33s$,$\theta_p = 15°$

In these works, the platform motions in time domain are synthesised as sinusoidal series at the first two dominant frequencies extracted from the simulation[5]. The time series of a particular platform motion is determined as

$$X(t) = X_0 + A_1 \sin(2\pi f_1 t + \phi_1) + A_2 \sin(2\pi f_2 t + \phi_2), \tag{66}$$

where the mean value X_0, amplitudes A_i, frequencies f_i and phase angles ϕ_i are given in Table 5.

Table 5. Parameters of platform motions[5] for a floating offshore wind turbine with different floater types.

Oper.	Platf.	Mode	X_0 $[m]/[°]$	A_1 $[m]/[°]$	f_1 $[Hz]$	ϕ_1 $[rad]$	A_2 $[m]/[°]$	f_2 $[m]/[°]$	ϕ_2 $[rad]$
1	ITI	surge	13.602	0.725	0.007	-1.163	-0.442	0.078	2.609
1	ITI	heave	-0.130	0.318	0.078	1.303	0.254	0.108	2.702
1	ITI	pitch	0.591	1.475	0.078	-0.066	1.630	0.083	1.816
1	OHS	pitch	1.580	-0.084	0.066	1.930	-0.116	0.077	3.113
1	OHS	yaw	-0.021	0.091	0.108	1.983	-0.036	0.120	3.429
1	TLP	surge	1.206	0.436	0.016	-0.831	-0.222	0.077	3.018
2	ITI	pitch	1.722	-0.637	0.065	-0.381	1.677	0.077	1.835
3	ITI	pitch	0.939	1.518	0.066	2.132	2.979	0.078	6.863
3	OHS	pitch	3.324	11.961	0.029	0.420	0.000	0.000	0.000
3	OHS	yaw	-0.222	2.000	0.029	-0.359	3.185	0.058	3.385

The mean μ_α and standard deviation σ_α of the angle of attack α on the outboard 2/3 of the blade are compared in Table 6. The current numerical results are presented in the column entitled 'FWVR2, tilt=0°', without shaft tilt angle. It is shown that μ_α and σ_α have the same trend than observed in the literature. In particular, μ_α is rather independent of the platform motion, for a given wind speed. The bottom-mounted monopile presents the smallest value of σ_α compared with floating support structures at the same wind speed. This can be explained by the fluctuations of the induced velocities caused by turbine-wake interactions in the floating case. The value of σ_α increases with the increase of platform motion. Also, the pitch motions of the platform tends to have more effect on the value of σ_α than the

surge motions, because the pitch motions generate shear wind velocities on the rotor. The values of μ_α are lower than the reference results throughout and the difference are within 1°, which is considered to be acceptable. The column 'FWVR2, tilt=5°' shows the α performance in the design condition of NREL5MW with a nonzero tilt angle. It can be seen that the values of μ_α are slightly lower than for zero tilt angle, which is mainly because the total wind area is smaller when the rotor is tilted. Moreover, σ_α is significantly influenced by the tilt angle in all cases because the latter can generate fluctuating streams especially on the outboard of the blades.

Table 6. Mean and standard deviation of α at the outboard 2/3 part of the blade.

			WInDS [5]		FWVR1[14]		FWVR2, tilt=0°		FWVR2, tilt=5°	
Operation	Platform	Mode	$\mu_\alpha[^\circ]$	$\sigma_\alpha[^\circ]$	$\mu_\alpha[^\circ]$	$\sigma_\alpha[^\circ]$	$\mu_\alpha[^\circ]$	$\sigma_\alpha[^\circ]$	$\mu_\alpha[^\circ]$	$\sigma_\alpha[^\circ]$
1	Monopile	–	3.95	0.23	3.86	0.48	3.82	0.15	3.71	3.23
1	ITI	surge	3.95	0.40	3.87	0.53	3.78	0.23	3.64	3.23
1	ITI	pitch	3.99	2.21	3.90	1.5	3.89	1.92	3.84	3.85
1	OHS	pitch	3.94	0.32	3.84	0.49	3.66	0.25	3.84	3.21
1	TLP	surge	3.95	0.27	3.86	0.49	3.64	0.23	3.70	3.23
2	Monopile	–	6.76	0.37	6.66	0.69	5.84	0.35	5.76	3.35
2	ITI	pitch	6.78	1.67	6.67	1.30	5.82	1.09	5.73	3.47
3	Monopile	–	-0.10	0.80	-0.31	2.24	-0.59	0.05	-0.61	2.91
3	ITI	pitch	-0.08	2.26	-0.28	2.88	-0.59	1.87	-0.61	3.39
3	OHS	pitch	-0.45	3.59	-0.52	3.09	-0.83	2.40	-0.85	3.57

The thrust force on the rotor for a bottom-mounted monopile in rated condition and five floating support structures in below-rated, rated and above-rated conditions are evaluated in time domain (Fig. 14) and frequency domain (Fig. 15). Figure 14 shows that the thrust curves fluctuate around their mean values, after an initial transient. The latter is due to the fact that a certain time is needed for the far-wake vortex rings to develop. Thus, initially, only the near wake mostly contributes to the values of induced velocities. After about 50 seconds, a steady-state is reached and statistics can be taken. Figure 15 highlights the dominant frequencies in the rotor thrust. For a bottom-mounted turbine on a monopile in rated conditions, the first dominant frequency is at about 0.6Hz, which corresponds to the vortex shedding frequency. Higher frequencies are multiples of the first one. This is due to a periodic process whereby the thrust force reaches a minimum value when the induced velocity reaches a peak value, and vice versa. For the FOWTs, without exception, the frequencies of the platform motions dominate in the frequency of the thrust force. This is because the velocities induced by the platform motions are larger than the induced velocities from the vortex rings.

Finally, we evaluate the blade bounded vortex strength Γ and its relationship with other parameters. As explained before, the value of Γ is obtained by equating the lift forces calculated from the 3D vortex lifting law and that from the blade element theory, see Eq (62). This leads to:

$$\Gamma = \frac{c}{2} C_l(\alpha) V^n, \tag{67}$$

where c is the constant chord length, C_l is the lift coefficient and V^n is the normal wind speed. The time evolutions of Γ, V^n, C_l and α are shown in Fig. 16, for the case of a floating wind turbine (OHS) above rated power. In each figure, the continuous line shows the platform pitching motion. The non-dimensional blade bound vortex strength $\Gamma/(\pi R V_\infty)$ (Fig. 16a) fluctuates regularly with the platform pitch motion. Also, the high-frequency oscillation with the period of about 4.96s is thought to be due to the rotor tilt angle. It can be seen that on the outboard of the blade, there are negative values of Γ, which is consistent with the negative values of α and C_l observed in the same conditions

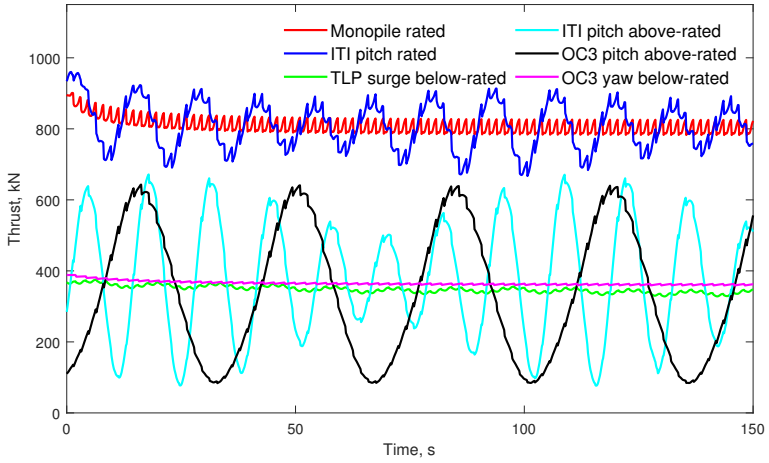

Figure 14. Time evolution of the thrust force on the rotor for different turbine configurations.

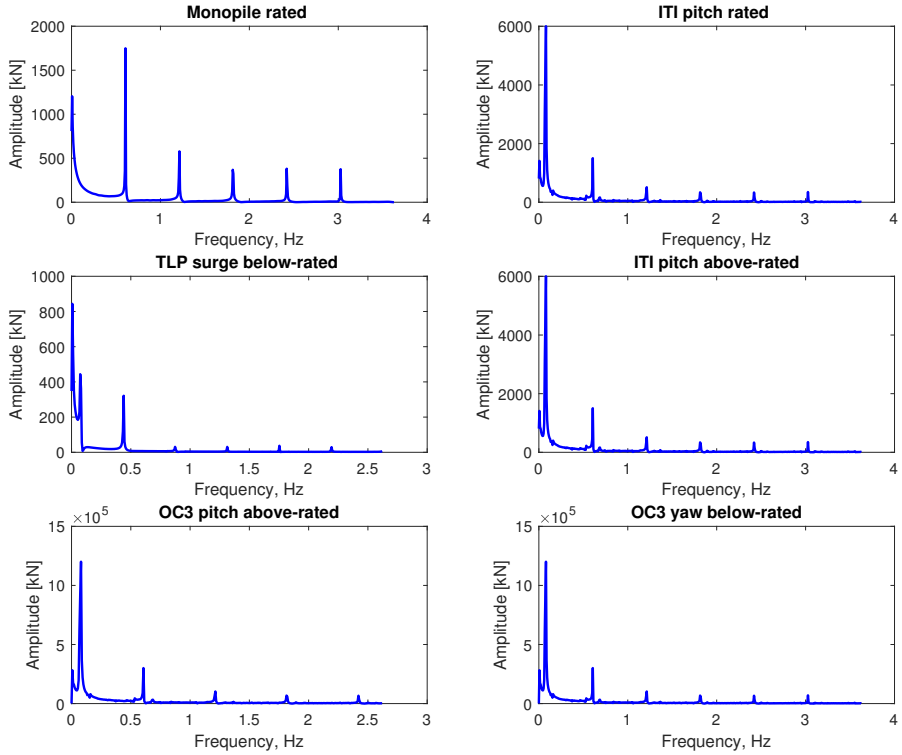

Figure 15. Frequency content of the thrust force on the rotor for different turbine configurations.

(Figs. 16c and 16d). The normal relative wind speed V^n is less influenced by the platform motion and the rotor tilt, its main fluctuations coming from the constant rotation of the rotor.

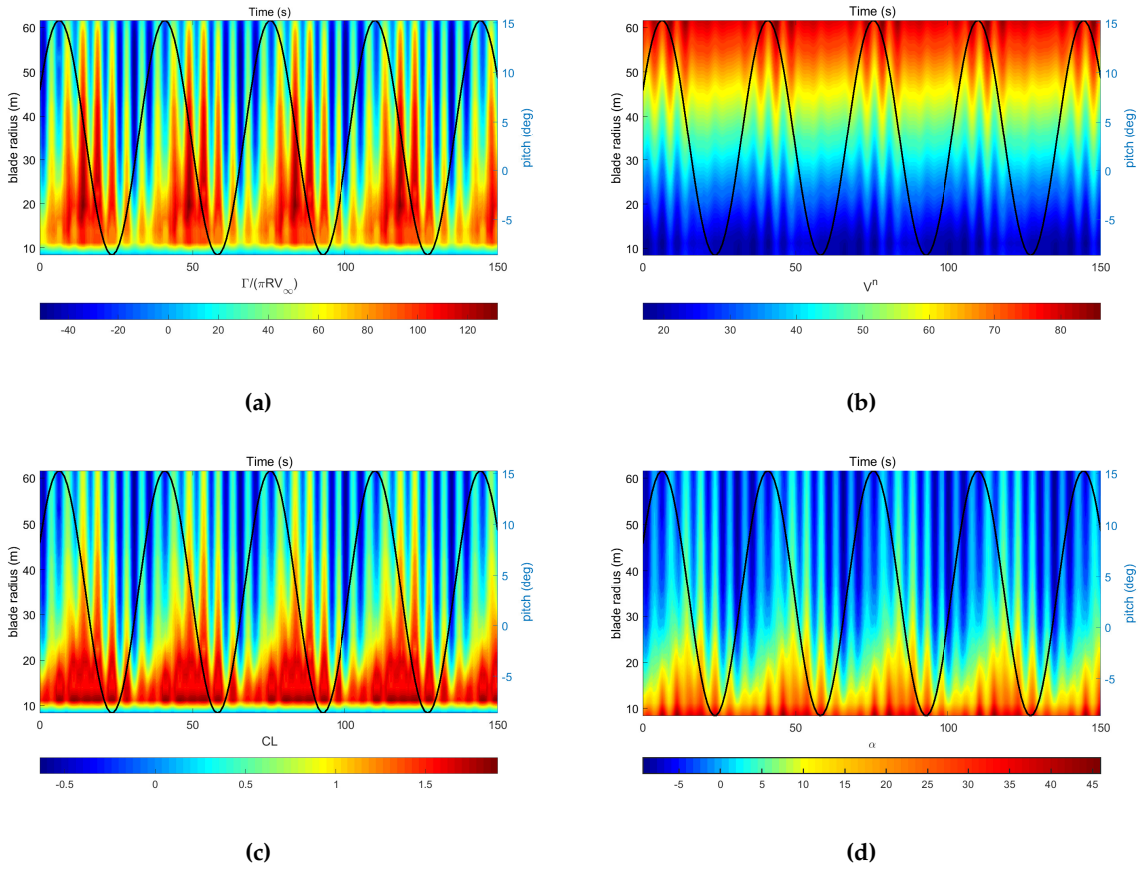

Figure 16. Time evolution of: (a) $\Gamma/(\pi RV_\infty)$, (b) V^n, (c) C_l and (d) α as a function of the location on the blade. The continuous line shows the pitching motion of the platform. Results are shown for the OHS above rated conditions.

5.3. Floating wind turbine under multiple-DoF motion

To conclude this results section, three multiple-DOF operating conditions are conducted, combining the properties listed in Table 5, namely:

1. Below-rated: The ITI Energy barge with platform surge, heave, and pitch DOFs.
2. Below-rated: The OC3-Hywind spar-buoy with platform pitch and yaw DOFs.
3. Above-rated: The OC3-Hywind spar-buoy with platform pitch and yaw DOFs.

The aerodynamic performance of a bottom-fixed wind turbine is also shown for comparison. The multiple-DoF motion thrusts of ITI Energy barge and OC3-Hywind spar with the below-rated operating conditions as well as the bottom fixed thrusts are compared with the results of Lee[6] in Fig. 17. It should be noted that the start time of the platform motions in the NVLM code and the present FWVR code are different. More specifically, the platform motions start at a zero azimuth angle in the FWVR code while they start approximately after one rotation of the rotor in the NVLM code. Therefore, In order to compare the thrusts of these two methods more clearly, the thrusts from the present FWVR method is shifted with $+360^\circ$ along the azimuth angle-axis. It is found that the bottom fixed thrust calculated with the present FWVR method is higher than the bottom fixed thrust calculated with the NVLM method, which is consistent with what has been observed in the two previous sections. Besides, the thrust amplitudes and frequencies obtained with both methods for the ITI Energy barge

and the OC3-Hywind spar platform match well. The wake induction at the rotor as a function of the downstream distance of the vortex rings are computed as a percentage of the total induced velocity at the rotor, and compared with Sebastian[5] in Fig. 18 for the ITI energy barge and in Fig. 19 for the OC3-Hywind spar-buoy with the NREL 5MW wind turbine. The blue dashed lines represent the contribution of the induced velocities from each section along the wake as obtained with the FWVF method, whilst the red lines are the results of the present FWVR method. The red circles on the line highlight the position of the vortex rings. The black lines and the green dotted lines represent the accumulated percentage of the induced velocities along the wake from the FWVF method and FWVR method, respectively. The induced velocity data output from the present FWVR method was captured at the operating time of 150s, when a stable condition was reached by the wind turbine. Since the convection of the vortex rings downstream is a dynamic process, the induced velocity captured at different time steps can be slightly different.

In general, the induced velocities are comparable between the two methods. As shown in Fig. 18, the accumulated percentage of the induced velocity at distances 1D and 2D behind the rotor differ only by 2%, and this difference decreases to maximum 1.0% as the distance behind the rotor increases. Furthermore, the induced velocities from each section along the wake show similar trend with both methods, the big fluctuations being mainly influenced by the platform motions, particularly from the pitch. For the OC3 platform below rated power (Fig. 19a), a similar discrepancy is observed between the models, with differences of 2.4% and 2.1% at distances of 1D and 2D behind the rotor and 0.6% further downstream. Also, the influence of the pitch and yaw platform motions on the induced velocity is relatively small. Above rated power (Fig. 19b), slightly larger discrepancies are observed, with differences of 9.8% and 4.8% at distances of 1D and 2D behind the rotor and less than 1% further downstream. Additionally, the present FWVR method predicts significantly larger contribution of the induced velocity from the vortex rings within the 1D distance downstream. This is mainly because the vortex rings convect faster with the increase in wind speed, and the density of rings is sparser at higher wind speed. Because the induced velocity is very sensitive to the distance between the control points and the vortex ring, see Eq. (24), the contribution from the front rings is much more significant than that of the rings further away from the rotor. The small differences in the results can be explained from the differences in wake induction of these two methods. The first difference is that the induced velocities of the wake from the FWVF method are output for each vortex segment in the wake, while the induced velocities from the present FWVR method are output for each vortex ring. As explained in Section 4, there are less vortex rings than vortex segments in the wake, thus the induced velocities of the wake from the FWVF method are relatively constant compared to those from the FWVR method. The second difference is that, due to the different modeling properties, the induced velocities from the FWVF method start from a position very close to the rotor, while the induced velocities from the present FWVR method start from the position of the first vortex ring, and the induced velocity at the rotor from the near wake model is not accounted here.

6. Conclusion

In this paper, a simplified free wake vortex ring method for horizontal-axis wind turbine was modified and assessed. Biot-Savart law was used for the near wake, while an analytical axis-symmetric vortex ring formulation was used for the far wake. A new trailed vortex model with finite length vortex lines was proposed in this paper. The NREL 5MW wind turbine was used to validate the code for the cases of monopile wind turbine, single-Dof platform motions and mutiple-Dof platform motions respectively. For the monopile wind turbine, the rotor thrust results showed good agreement between the other aerodynamic models for a large range of wind speeds. At low and high wind speeds, the results suggested that the present free wake vortex ring method is more reliable than BEM when calculating the rotor thrust. The method was applied to floating offshore wind turbines at below-rated, rated and above-rated conditions. For the single-Dof platform motions it was found that the mean and standard deviations of angle of attack at the outboard 2/3 part of the blade are

Preprints (www.preprints.org) | NOT PEER-REVIEWED | Posted: 6 August 2019 doi:10.20944/preprints201908.0078.v1

Peer-reviewed version available at Energies 2019, 12, 3900; doi:10.3390/en12203900

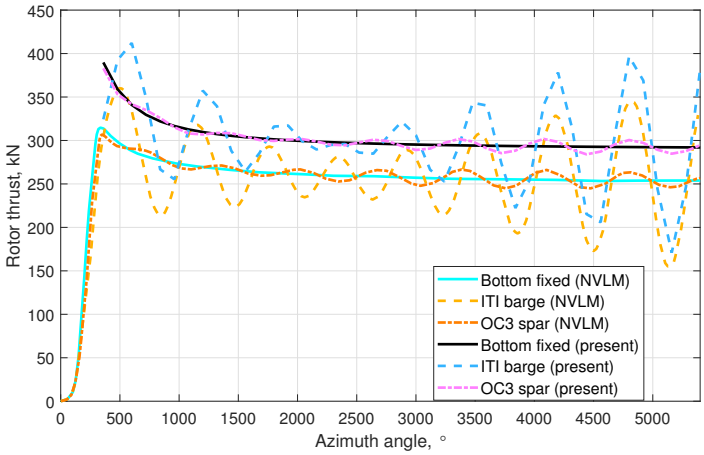

Figure 17. Variation in the thrust of 5MW NREL wind turbine in multiple-DoF motions.

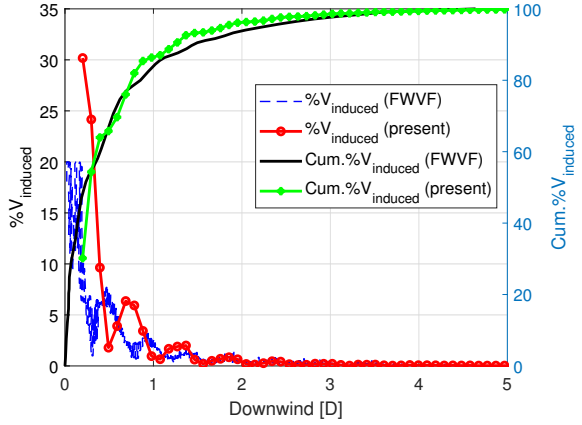

Figure 18. Wake induced velocity at the rotor for the NREL-5MW turbine + ITI Energy barge under platform surge, heave, and pitch for below-rated operating conditions.

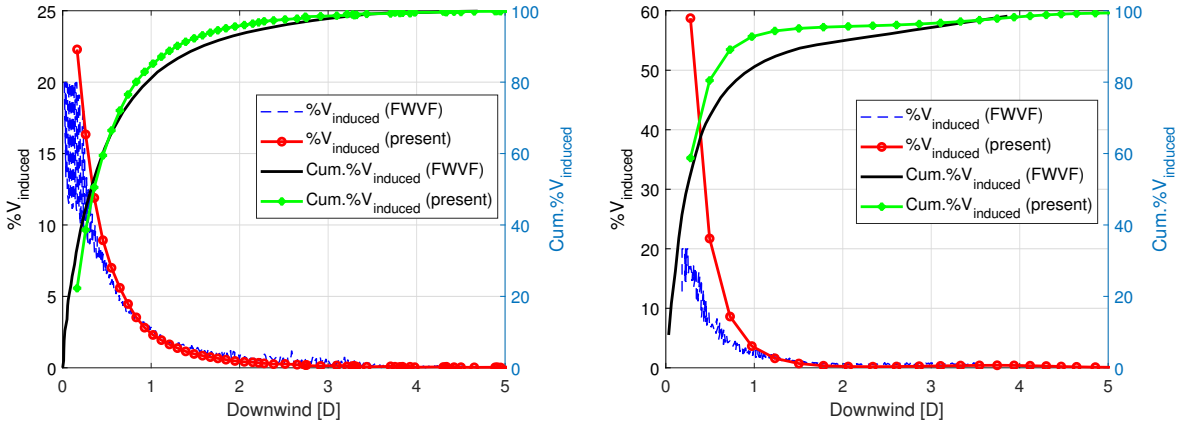

Figure 19. Wake induced velocity at the rotor for the NREL-5MW turbine + OC3-Hywind spar-buoy under platform pitch and yaw. (a) Below-rated; (b) Above-rated.

comparable with the literature. Also, the rotor tilt angle seemed to significantly influence the standard deviation of the angle of attack. The analysis of the thrust force on the rotor showed that its first dominant frequency for a monopile support structure is dominated by the vortex shedding frequency, whilst its first dominant frequency for floating support structures is driven by the platform motion. Also, the latter influence the lift coefficient on the rotor, and hence, the blade bound vortex strength. For the mutiple-Dof platform motions the results of rotor thrust as well as the induced velocities in the wake showed good agreement with the FWVF model.To conclude, the modified free wake vortex ring method proposed here is considered to be effective and reliable when solving the aerodynamic load around horizontal-axis wind turbines, both on fixed and floating support structures. It can be used to calculate conditions of small angles of attack at low wind speeds, small angles of attack due to blade pitch motion at high wind speeds, and varying angles of attack due to unsteady wind flows in the context of floating offshore wind turbines.

Author Contributions: conceptualization, J.D. and A.V.; methodology, J.D.; software, J.D.; validation, J.D., A.V. and C.S.F.; formal analysis, J.D.; investigation, J.D.; resources, Z.R.L.; data curation, J.D.; writing–original draft preparation, J.D.; writing–review and editing, A.V. and C.S.F.; visualization, J.D. and Z.R.L.; supervision, A.V. and G.B.; project administration, A.V.; funding acquisition, J.D., A.V. and G.B.

Funding: This research was funded by China Scholarship Council (CSC).

Acknowledgments: Dong would like to acknowledge support from China Scholarship Council (CSC), Viré acknowledges support from the Rijksdienst voor Ondernemend Nederland (RVO) through the TSE Hernieuwbare Energie funding scheme (ABIBA project). Many thanks are also extended to Jacobus B. de Vaal of the Institute for Energy Technology in Norway for his generous assistance in this work.

Conflicts of Interest: The authors declare no conflict of interest. The funders had no role in the design of the study; in the collection, analyses, or interpretation of data; in the writing of the manuscript, or in the decision to publish the results.

Abbreviations

The following abbreviations are used in this manuscript:

FOWT	Floating Offshore Wind Turbines
BEM	Blade Element Momentum Theory
CFD	Computational Fluid Dynamics
NREL	National Renewable Energy Laboratory
FWVF	Free Wake Vortex Filament Method
NVLM	Nonlinear Vortex Lattice Method
FWVR	Free Wake Vortex Ring Method
OC3	Code Comparison Collaboration
OHS	OC3-Hywind Spar-Buoy
TLP	Tension Leg Platform
RANS	Reynolds-averaged Navier–Stokes Method
AFWRV	Actuator Disc with Free Wake Vortex Ring Model

1. Sebastian, T.; Lackner, M. Characterization of the unsteady aerodynamics of offshore floating wind turbines. *Wind Energy* **2013**, *16*, 339–352. doi:10.1002/we.545.
2. Emmanuel, B. *Wind Turbine Aerodynamics and Vorticity-Based Methods, Fundamentals and Recent Applications*; Springer, 2017.
3. Bhagwat, M.; Leishman, J. Transient Rotor Inflow Using a Time-Accurate Free-Vortex Wake Model. *AIAA, Aerospace Sciences Meeting and Exhibit* **2001**. doi:10.2514/6.2001-993.
4. Gohard, J.C. Free wake analysis of wind turbine aerodynamics. Technical report, MIT, 1978.
5. Sebastian, T.; Lackner, M. Analysis of the Induction and Wake Evolution of an Offshore Floating Wind Turbine. *Energies* **2012**, *5*, 968–1000. doi:10.3390/en5040968.

6. Lee, H.; Lee, D.J. Effects of platform motions on aerodynamic performance and unsteady wake evolution of a floating offshore wind turbine. *Renewable Energy* **2019**, *143*, 9 – 23. doi:https://doi.org/10.1016/j.renene.2019.04.134.
7. Newman, S. The induced velocity of a vortex ring filament. AFM Technical Reports 11/03, University of Southampton, School of Engineering Sciences, 2011.
8. Yoon, S.; Heister, S. Analytical formulas for the velocity field induced by an infinitely thin vortex ring. *International Journal for Numerical Methods in Fluids* **2004**, *44*, 665–672. doi:10.1002/fld.666.
9. Ø ye, S. A simple vortex model. *In Proc. of the third IEA Symposium on the Aerodynamics of Wind Turbines , ETSU, Harwell* **1990**.
10. de Vaal, J.; Hansen, M.; Moan, T. Validation of a vortex ring wake model suited for aeroelastic simulations of floating wind turbines. *Journal of Physics: Conference Series* **2014**. doi:10.1088/1742-6596/555/1/012025.
11. Yu, W.; Ferreira, C.S.; van Kuik, G.; Baldacchino, D. Verifying the Blade Element Momentum Method in unsteady, radially varied, axisymmetric loading using a vortex ring model. *Wind Energy* **2017**, *20*, 269–288. doi:https://doi.org/10.1002/we.2005.
12. Miller, R. Simplified Free Wake Analysis for Rotors. Technical report, Aeronautical Research Inst. of Sweden, Stockholm.; National Aeronautics and Space Administration, Washington, DC., 1982.
13. Afjeh, A. Wake effects on the aerodynamic performance of horizontal axis wind turbines **1984**.
14. de Vaal, J.; Hansen, M.; Moan, T. Influence of Rigid Body Motions on Rotor Induced Velocities and Aerodynamic Loads of a Floating Horizontal Axis Wind Turbine. *ASME. International Conference on Offshore Mechanics and Arctic Engineering* **2014**, *9B: Ocean Renewable Energy*. doi:10.1115/OMAE2014-24227.
15. de Vaal, J. Aerodynamic modelling of floating wind turbines. Thesis for the degree of philosophiae doctor, NTNU, Trondheim, 2015.
16. Leonard, A. Computing Three-Dimensional Incompressible Flows with Vortex Elements. *Annual Review of Fluid Mechanics* **1985**, *17*, 523–559. doi:10.1146/annurev.fl.17.010185.002515.
17. van Hoydonck, W.; Gerritsma, M.; van Tooren, M. On Core and Curvature Corrections used in Straight-Line Vortex Filament Methods. *submitted for review to the Journal of the American Helicopter Society* **2012**, p. 34.
18. Betz, A. Behavior of Vortex Systems. Technical Reports NACA-TM-713, National Advisory Committee for Aeronautics, 1993.
19. Phillips, WF.and Snyder, D. Modern Adaptation of Prandtl's Classic Lifting-Line Theory. *Journal of Aircraft* **2000**, *34*, 622–670. doi:10.2514/2.2649.
20. Faltinsen, O. *Sea Loads on Ships and Offshore Structures*; Cambridge University Press, 1993.
21. van Garrel, A. Requirements for a Wind Turbine Aerodynamics Simulations Module - Version 1 **2001**.
22. Jonkman, J .and Butterfield, S.; Musial, W.; Scott, G. Definition of a 5-MW Reference Wind Turbine for Offshore System Development. Technical report, NASA, 1981.
23. Vaz, J.; Pinho, J.; Mesquita, A. An extension of BEM method applied to horizontal-axis wind turbine design. *Renewable Energy* **2011**, *36*, 1734–1740. doi:https://doi.org/10.1016/j.renene.2010.11.018.
24. Rahimi, H.; Dose, B.; Stoevesandt, B.; Peinke, J. Investigation of the validity of BEM for simulation of wind turbines in complex load cases and comparison with experiment and CFD. *Journal of Physics: Conference Series* **2016**, *749*. doi:10.1088/1742-6596/749/1/012015.